Vibration Control Under Frequency-Varying Disturbances With Application to Satellites

Bloemers, Tom; Leemrijse, Sjoerd; Preda, Valentin; Boquet, Fabrice; Oomen, Tom; Toth, Roland

DOI
10.1109/TCST.2024.3384896

Publication date
2024

Document Version
Final published version

Published in
IEEE Transactions on Control Systems Technology

Vibration Control Under Frequency-Varying Disturbances With Application to Satellites

Tom Bloemers, Sjoerd Leemrijse, Valentin Preda, Fabrice Boquet, Tom Oomen, *Senior Member, IEEE*, and Roland Tóth, *Senior Member, IEEE*

***Abstract*— Increasing demands of positioning accuracy of satellites with high-precision payloads together with growing structural flexibility of their hulls, calls for active vibration isolation techniques to mitigate the impact of microvibrations on the payload. The aim of this article is to develop an linear parameter-varying (LPV) modeling and control design methodology for attenuation of frequency-varying disturbances. Application of the developed approach to a realistic space-capable multivariable vibration isolation test-bench setup shows a significant attenuation of microvibration disturbances, well-demonstrating the capabilities and deployability of the proposed method.**

***Index Terms*— Linear parameter-varying (LPV) systems, satellites, vibration control.**

I. Introduction

MODERN space observation missions require extremely challenging accuracy requirements. All around the globe in outer space, satellites orbit the Earth to facilitate a variety of services to mankind, e.g., navigation, communication, meteorology, observation, and more. Examples include cosmic vision missions, such as the James Webb Telescope as well as low-Earth orbit missions such as the Sentinel satellites [1]. A large portion of these satellites carry optical instruments to make images of Earth's surface or other celestial objects. Over the years, there has been an growing demand on the resolution of these images [2]. With such an increase in performance requirements, mechanical vibrations have become a key factor in image degradation.

Microvibrations severely degrade image quality by introducing image distortions and blurring effects [3]. Besides of vibrations induced by on-board equipment, such as solar panel arrays, thrusters, and cryocoolers, the predominant source of microvibrations is the *attitude control system* (ACS). The ACS consists of reaction wheel assemblies or control moment gyroscopes, which are used to point the satellite in the desired direction. These components are manufactured with extremely high precision, yet microvibrations originating from them are unavoidable due to static and dynamic unbalances in the flywheels and imperfections in the bearings [4], [5]. These disturbances depend on the rotational frequency of the flywheels and therefore span a broad frequency range. At the same time, for economic and logistic reasons, satellites are becoming more and more lightweight, causing the hull of the spacecraft to become a flexible body. As a result, microvibrations are significantly amplified by the lightweight and flexible hull and become a key performance limiting factor.

In the past, state-of-the-art microvibration isolation solutions based on passive isolators have been able to provide sufficient suppression; however, with the next-generation satellite designs, these technologies are reaching their physical limitations. Passive approaches use stiffness and damping elements to dissipate the vibrational energy as heat and typically they involve placing isolators between the disturbance source and the optical equipment, constructed from viscoelastic materials, springs, or hydraulic dampers [6]. These isolators act as a low-pass filter, suppressing disturbances in the higher frequency ranges only. In some cases, a posteriori image processing algorithms can correct for some of the remaining image distortions. Nonetheless, artifacts such as blurring and disturbances in the low-frequency range are not corrigible. In addition, passive isolators leave underdamped modes at low frequencies, where microvibration disturbances are expected. Therefore, current state-of-the-art vibration isolation techniques are insufficient to meet the increasing accuracy requirements.

To overcome the limitations of passive isolation techniques and to achieve vibration isolation in a broad frequency spectrum, future satellites will need to be equipped with a hybrid vibration isolation platforms [7], [8]. Hybrid vibration isolation combines passive isolators with active components,

Manuscript received 13 January 2024; accepted 9 March 2024. Date of publication 23 April 2024; date of current version 23 October 2024. This work was supported in part by European Research Council (ERC) through European Union's Horizon 2020 Research and Innovation Programme under Grant 714663 and in part by European Space Agency (ESA) through the Open Space Innovation Platform Research Programme under Contract 4000133755/21/NL/MH/hm. Recommended by Associate Editor J.-W. van Wingerden. *(Corresponding author: Tom Bloemers.)*

Tom Bloemers is with the Control Systems Group, Department of Electrical Engineering, Eindhoven University of Technology, 5612 AZ Eindhoven, The Netherlands (e-mail: t.a.h.bloemers@tue.nl).

Sjoerd Leemrijse is with Sioux Technologies, 5633 AA Eindhoven, The Netherlands (e-mail: sjoerd.leemrijse@sioux.eu).

Valentin Preda and Fabrice Boquet are with European Space Agency (ESA/ESTEC), 2200 AG Noordwijk, The Netherlands (e-mail: valentin.preda@esa.int; fabrice.boquet@esa.int).

Tom Oomen is with the Control Systems Technology Group, Department of Mechanical Engineering, Eindhoven University of Technology, 5612 AZ Eindhoven, The Netherlands, and also with Delft Center for Systems and Control, Faculty of Mechanical, Maritime and Materials Engineering (3 mE), TU Delft, 2628 CD Delft, The Netherlands (e-mail: t.a.e.oomen@tue.nl).

Roland Tóth is with the Control Systems Technology Group, Department of Electrical Engineering, Eindhoven University of Technology, 5612 AZ Eindhoven, The Netherlands, and also with the Systems and Control Laboratory, Institute for Computer Science and Control, 1111 Budapest, Hungary (e-mail: r.toth@tue.nl).

Digital Object Identifier 10.1109/TCST.2024.3384896

which consist of sensors and actuators, typically arranged in a hexapod configuration similar to a Stewart platform [9]. These actuators are used to generate forces that can counteract vibration disturbances. Simulation studies on satellites equipped with flexible appendages and ACSs has shown the effectiveness of the proposed solution and the promising performance improvement that can be achieved by it [1], [10].

When the source of the vibration disturbances is unknown, *linear time-invariant* (LTI) compensation and adaptive control provide powerful tools for active vibration control, see [11], [12]. Effectiveness of these methods has been well demonstrated in a variety of practical examples. However, the LTI tools cannot cope with time-varying disturbances, whereas adaptive tools are based on recursive adaption of the controller with manually tuned adaptation gains for which stability and convergence guarantees are difficult to obtain. Furthermore, for satellites, variation of the microvibrations is related to known/measurable rotational speed of the generating equipment (flywheels and solar arrays) that can be exploited for improved mitigation performance. In fact, varying-frequency nature of microvibration disturbances allows to interpret them as signals generated by *linear parameter-varying* (LPV) filters. In this sense, the disturbances are modeled with a linear *input–output* (IO) map, whose dynamics depend on the exogenous frequency variations of the modeled microvibrations. The LPV framework has been developed to provide systematic design tools for the analysis and synthesis of LPV controllers for nonlinear systems [13], [14]. Hence, compared with the adaptive and LTI disturbance rejection methods, this framework enables the design of LPV controllers scheduled by frequency variations of the disturbances to efficiently achieve broadband microvibration isolation under stability and performance guarantees and systematic performance tuning.

The LPV framework has been already investigated in the context of vibration control. In [15] and [16], a scheduled controller synthesis approach for asymptotic regulation against nonstationary sinusoidal disturbances has been worked out. In [17], [18], and [19], the internal model principle is utilized to design controllers to reject frequency-varying harmonic disturbances. Specifically for satellites, a signal-based LPV control design approach has been presented[1] in [1] and [10]. While effectiveness of these methods has been successfully demonstrated through various simulation studies, experimental demonstration of the technology has not been achieved before. Furthermore, these approaches have been derived for designing *continuous-time* (CT) controllers for known or partly known system models with predescribed uncertainty ranges neither investigating the necessary toolchain required for their applicability nor their implementation on digital hardware, in which naive discretization of the controllers often results in frequency distortions that are intolerable for precise rejection of varying harmonic disturbances in space.

[1]Previously in the LPV context, microvibration isolation was studied with the goal to reduce transmitted forces and torques between the wheel and the satellite platform. In our considered isolator setting, the goal is to reduce the payload acceleration from base vibrations, which is a different problem.

Although the LPV framework provides a systematic toolchain to design controllers for rejection of frequency-varying harmonic disturbances, a full design framework from experimental modeling toward full-scale implementation is presently lacking. In this respect, the main contribution of this article is a complete design and validation approach for rejection of varying harmonic microvibration disturbances with application to a realistic state-of-the-art microvibration isolation test platform. This is achieved through the following subcontributions.

C1: A novel LPV disturbance modeling and control design methodology for attenuation of slowly varying multiple microvibrations whose frequency is known or measurable and a discretization approach to preserve the harmonic attenuation performance when the controllers are implemented on digital hardware.

C2: Implementation and thorough validation of the methodology on a *multiple input multiple output* (MIMO) vibration isolation test bench setup, including full-scale system identification of the IO dynamics.

The benefits of this approach include an easy-to-automate data-driven modeling step to capture the isolator dynamics and avoid complicated, first-principles-based modeling of the system. This is combined with a relatively simple microvibration disturbance model. The control design is achieved through a well-known mixed-sensitivity shaping approach, see [20], [21], in which the parameter-varying harmonic disturbances are translated to constraints on the sensitivity functions. Furthermore, we show how to apply a modified Tustin discretization method for LPV controllers, which by varying the prewarping frequency preserves local resonance/suppression modes of the CT controllers in *discrete time* (DT).

This article is organized as follows. In Section II, the vibration isolation problem is formulated together with the characterization of the microvibration disturbances and the concept of disturbance modeling. Furthermore, the prototype setup for experimental validation is introduced. In Section III, an identification procedure to experimentally model the actuator dynamics in terms of their vibration mitigation at the point-of-interest is proposed. This is followed by proposing an LPV controller design procedure to achieve active vibration isolation in Section IV. Together, these sections form Contribution C1. Furthermore, in Section IV, we discuss implementation of the controllers via a modified Tustin discretization method, which preserves the local resonance modes of the designed controller. In Section V, application and experimental validation of the presented methodology on a prototype vibration isolation setup is shown (Contribution C2). Finally, an overview of the procedure is given and conclusions on the achieved results are drawn in Section VI.

Notation: Let $\mathbb{R}$ and $\mathbb{R}_+$ be the set of real and nonnegative real numbers while $\mathbb{C}$ stands for the set of complex numbers. $\mathbb{R}^n$ ($\mathbb{C}^n$) denotes the set of n-dimensional real (complex) vectors while $\mathbb{R}^{n\times m}$ ($\mathbb{C}^{n\times m}$) stands for the set of real (complex) $n \times m$ matrices. $\mathcal{L}_2^n$ is used for $\mathbb{R}_+ \to \mathbb{R}^n$ square integrable signals, i.e., with finite $\|f\|_2 = (\int_0^\infty \|f(t)\|^2 dt)^{1/2}$, where $\|\cdot\|$ is the Euclidean norm. $\mathcal{L}_{2e}^n$ denotes the extended $\mathcal{L}_2^n$ space of functions with a finite $(\int_0^T \|f(t)\|^2 dt)^{1/2}$ for any $T > 0$. For

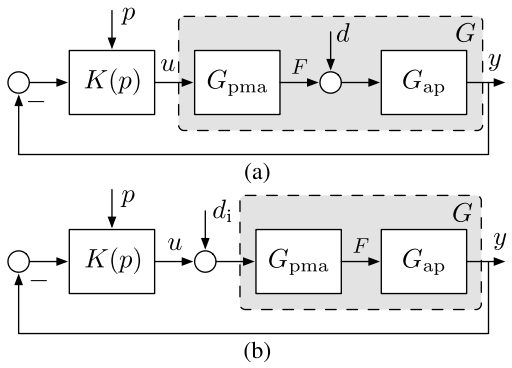

Fig. 1. Control architecture for the vibration isolation setup. Here, G_{ap} and G_{pma} represent the active plate and the PMA dynamics, while K is the to-be-designed LPV controller. The system is subject to (a) microvibration disturbance forces d, which are replicated by (b) PMA disturbance voltages d_i.

appropriately dimensioned matrices

$$N = \begin{bmatrix} N_{11} & N_{12} \\ N_{21} & N_{22} \end{bmatrix}, \quad M = \begin{bmatrix} M_{11} & M_{12} \\ M_{21} & M_{22} \end{bmatrix}$$

the Redheffer star product $N \star M$ is defined as $N \star M =$

$$\begin{bmatrix} \mathcal{F}_l(N, M_{11}) & N_{12}(I - M_{11}N_{22})^{-1}M_{12} \\ M_{21}(I - N_{22}M_{11})^{-1}N_{21} & \mathcal{F}_u(M, N_{22}) \end{bmatrix}$$

where $\mathcal{F}_l(N, V) = N_{11} + N_{12}V(I - N_{22}V)^{-1}N_{21}$ is the lower *linear fractional transformation* (LFT), while $\mathcal{F}_u(M, V) = M_{22} + M_{21}V(I - M_{11}V)^{-1}M_{12}$ stands for the upper LFT, assuming that the corresponding matrix inverses exist. Furthermore, let $\mathbb{I}_{\tau_1}^{\tau_2} = \{k \in \mathbb{Z} \mid \tau_1 \leq k \leq \tau_2\}$ be an index set.

II. System Description and Problem Formulation

A. Vibration Isolation Problem Description

In this section, we introduce the general hybrid vibration isolation problem and the proposed control architecture. A hybrid isolation setup consists of a platform that is connected to the environment, and mounted with sensitive measurement equipment, passive isolators, and actuators. The platform and the equipment are subject to exogenous vibrations originating from the environment, generating undesired disturbance forces that impact the performance of the measurement equipment.

To that end, consider the platform $G_{\text{ap}}\colon \begin{bmatrix} F^\top & d^\top \end{bmatrix}^\top \mapsto y$ with actuator forces $F(t) \in \mathbb{R}^{n_u}$, vibrational disturbance forces $d(t) \in \mathbb{R}^{n_u}$, and measured output $y(t) \in \mathbb{R}^{n_y}$, e.g., the acceleration of the point of interest. The idea behind active vibration isolation is to generate forces F, typically generated by electromechanical actuators, e.g., *proof mass actuators* (PMAs) $G_{\text{pma}}\colon u \mapsto F$, to counteract the disturbance forces d, such that the effect of the vibrations on the platform is minimized. As aforementioned, and further specified in Section II-B, microvibration disturbances can be modeled in the LPV framework. Therefore, we propose the control architecture depicted in Fig. 1(a), where the objective is to design an LPV controller that counteracts the vibration disturbances. The characteristics of these disturbances are described in Section II-B.

B. Disturbance Model

There are multiple components in a satellite that can cause microvibration disturbance forces. For example, cryocoolers or reaction wheels that are part of the ACS. These vibrations travel through the body of the spacecraft toward the platform on which the payload is mounted. To ensure the performance of the payload, it is necessary to isolate it from microvibration disturbances. Microvibrations are mainly characterized by their harmonic components. For space applications, often harmonic content of the disturbances is partly known. For example, in the case of a reaction wheel assemblies, the rotational speed of the reaction wheel directly influences the frequency of the disturbance vibrations, where the main harmonic has the same frequency as the rotational speed of the wheel [4], [5]. The same partial knowledge is also present for other components.

To incorporate this information in our problem setting, we consider a general disturbance model that can describe mechanical vibrations, originating from a variety of sources, in terms of the force and torque disturbance vector $d(t) \in \mathbb{R}^{n_u}$

$$d(t) = d_{\text{bn}}(t) + \sum_{i=1}^{N_d} d_{h,i}(t) \tag{1}$$

where $d_{\text{bn}}(t) \in \mathbb{R}^{n_u}$ represents the stochastic broadband noise component of the disturbance and $d_{h,i}(t) \in \mathbb{R}^{n_u}$ represents the ith harmonic component with

$$d_{h,i}(t) = A_i(\Omega(t)) \sin(2\pi\Omega(t)h_i t + \phi_i), \quad i \in \mathbb{I}_1^{N_d} \tag{2}$$

where $\Omega(t) \in \boldsymbol{\Omega} \subset \mathbb{R}$ is the frequency of the main harmonic component, $h_i \in \mathbb{R}$ is the order of the harmonic component, $\phi_i \in \mathbb{R}^{n_u}$ is the phase angle, and $A_i(\Omega(t)) \in \mathbb{R}^{n_u}$ is the amplitude. For the first harmonic component, $h_1 = 1$. According to our application setting, we consider the variation of the main harmonic component $\Omega(t)$ to be measurable.

The varying-frequency nature of the microvibration disturbances allows them to be interpreted as outputs of a parameter-varying disturbance generator. In this sense, the ith harmonic disturbance is modeled by

$$d_{h,i}(t) = A_i(p(t)) \sin(2\pi p(t)h_i t + \phi_i) \tag{3}$$

with $p(t) \in \mathbb{P} \subset \mathbb{R}^{n_p}$ the scheduling variable, describing the main harmonic of the disturbance, i.e., $p = \Omega$. Throughout this article, we assume that the change of the main harmonic, i.e., $\dot{p} = \dot{\Omega}$, is sufficiently slow, such that the momentary frequency content of (2) is dominated by the sinusoidal component instead of the time variation of $\Omega(t)$. This is in-line with space applications, where the variation of the disturbance dynamics is typically much slower than the considered frequency range in which the disturbance acts.

C. Vibration Isolation Test Platform

To show effectiveness of the to-be-proposed design methodology, we consider the active vibration isolation setup depicted in Fig. 2. The setup is a prototype platform of the isolation architecture described in [10]. The setup consists of three distinctive parts, namely: 1) an optical table; 2) an active plate; and 3) a dummy mass. This is schematically depicted in Fig. 2.

The optical table is suspended via air mounts, see [22], from the ground and can be seen as the body of a spacecraft in microgravity. Mounted on the top of the optical table is an aluminum disk, which is the active plate, supporting six PMAs, and an *inertial measurement unit* (IMU). Rubber-based passive isolators are set between the optical table and the active plate, representing the connection between a satellite body and the vibration isolation table with optical instruments. Together, the passive isolator joints create a virtual six *degrees of freedom* (DoFs) joint around which the active plate translates and rotates. The three translational three rotational accelerations are measured by the IMU, which provides information about the disturbances experienced by the payload. A dummy mass is rigidly mounted on the active plate to represent a typical space payload, e.g., sensitive optical instruments or microvibration inducing equipment. The six PMAs mounted on the plate in a hexapod configuration and exert three forces and three torques in all six DoF of the plate to enable active vibration isolation. The PMAs are controlled via a microcontroller (Raspberry PI 4). The microcontroller generates digital commands to an electronic board with a multichannel *digital-to-analog converter* (DAC) followed by low pass filters and amplifiers. The amplifiers are connected to the 6× PMAs. The microcontroller has a relatively low sampling/control frequency of 8.235 and serves as a limited computing resource, being representative of the computing resources found in space equipment. Due to reasons of confidentiality, throughout this article, the time and frequency axes have been normalized by an affine transformation, resulting in dimensionless quantities.

To give an indication of the general motion dynamics of the system and what is considered to be inputs and outputs, we derive a simple ideal motion model of the system. Note that in reality, the dynamics of such a system are much more complex, but we present an idealistic model here to provide an understanding of how the forces and torques between different components are related. Later, in Section III, we identify the end-to-end dynamics of the vibration isolation setup. The ideal dynamics of the vibration isolation test platform can be characterized by the interconnection of the active plate with passive isolators and electromechanical PMAs. The plate has the following ideal LTI dynamics

$$G_{\text{ap}}: \begin{cases} \mathcal{M}_{\text{ap}}\ddot{q}(t) + \mathcal{C}_{\text{ap}}\dot{q}(t) + \mathcal{K}_{\text{ap}}q(t) = \mathcal{F}(F(t) + d(t)) \\ y(t) = \ddot{q}(t) \end{cases} \tag{4}$$

where $\ddot{q}(t) \in \mathbb{R}^{n_y}$ with $\ddot{q} = \begin{bmatrix} \ddot{x} & \ddot{y} & \ddot{z} & \ddot{\theta}_x & \ddot{\theta}_y & \ddot{\theta}_z \end{bmatrix}^\top$ represents the translational and rotational accelerations of the plate, $F = \begin{bmatrix} F_x & F_y & F_z & \tau_x & \tau_y & \tau_z \end{bmatrix}^\top$ with $F(t) \in \mathbb{R}^{n_u}$ represents the PMA forces and torques, and $d(t) \in \mathbb{R}^{n_u}$ is the collection of the micro-vibration disturbance forces and torques acting on the plate. Here, $\mathcal{M}_{\text{ap}}$, $\mathcal{C}_{\text{ap}}$, $\mathcal{K}_{\text{ap}}$, and $\mathcal{F}$ are the active plate mass and inertia, damping, stiffness, and input matrices, respectively. The ideal dynamics of the PMAs are described by the LTI model

$$G_{\text{pma}}: \begin{cases} \mathcal{M}_{\text{pma}}\ddot{x}(t) + \mathcal{C}_{\text{pma}}\dot{x}(t) + \mathcal{K}_{\text{pma}}x(t) = K_m i(t) \\ K_m\dot{x}(t) + L\dot{i}(t) + Ri(t) - d_i(t) = u(t) \\ -\mathcal{M}_{\text{pma}}\ddot{x}(t) = F(t) \end{cases} \tag{5}$$

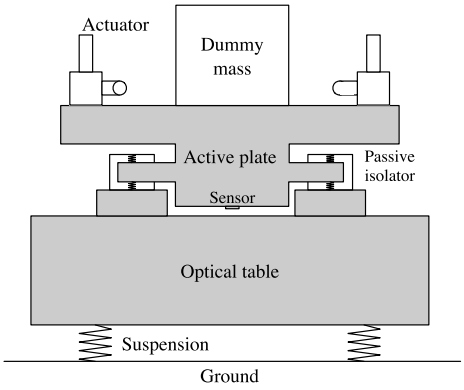

Fig. 2. Schematic of the vibration isolation setup with its components.

where $x(t) \in \mathbb{R}^{n_u}$ is the translation of the proof-masses, $i(t) \in \mathbb{R}^{n_u}$ is the current flowing through the PMAs, $u(t) = \begin{bmatrix} u_1(t) & \cdots & u_6(t) \end{bmatrix}^\top \in \mathbb{R}^{n_u}$ is the voltage applied to the PMAs, and similarly $d_i(t) \in \mathbb{R}^{n_u}$ are the disturbance voltages of the PMAs. Here, $\mathcal{M}_{\text{pma}}$, $\mathcal{C}_{\text{pma}}$, and $\mathcal{K}_{\text{pma}}$ are the PMA mass, damping, and stiffness matrices, respectively, while K_m, L, and R are the motor constant, inductance, and resistance, respectively.

The passive isolators are used to attenuate the effect of high-frequent disturbances on the active plate. Therefore, active rejection of low-frequency microvibration disturbances is targeted by actuating the six PMAs. In a real-world system, the component that carries sensitive measurement equipment in the satellite is attached to the top of the active plate. Isolating the plate from vibrations, therefore, indicates how well vibrations are mitigated w.r.t. the measurement equipment. To emulate microvibrations traveling through the satellite body to the isolator platform, input disturbance voltages d_i with similar characteristics as in Section II-B are introduced with harmonic component $\Omega(t) \in \boldsymbol{\Omega} = [0.59, 1.07]$ and $|\dot{\Omega}(t)| \leq 0.01$.

D. Problem Formulation

The goal of the control system is to isolate the payload from the satellite base vibrations. If the vibrations are minimized, then the payload accelerations are also reduced. In this application, we consider control of the rotational accelerations only, i.e., $G: \begin{bmatrix} u_1 & \cdots & u_6 \end{bmatrix}^\top \mapsto \begin{bmatrix} \ddot{\theta}_x & \ddot{\theta}_y & \ddot{\theta}_z \end{bmatrix}^\top$. Furthermore, in our setup, the input of PMA 2 is also used to inject the microvibration disturbances.

The challenge is to design an active vibration isolation strategy that guarantees stability and performance for the considered microvibrations dependent on $\Omega(t) \in \boldsymbol{\Omega}$. For this purpose, we consider to design an LPV controller $K(p(t))$ scheduled by the main harmonic component $p(t) = \Omega(t)$.

The considered LPV controller admits the state-space representation

$$\dot{x}_k(t) = A_k(p(t))x_k(t) + B_k(p(t))u_k(t) \tag{6a}$$

$$y_k(t) = C_k(p(t))x_k(t) + D_k(p(t))u_k(t) \tag{6b}$$

where $x_k(t) \in \mathbb{R}^{n_x}$ denotes the state, $y_k(t) \in \mathbb{R}^{n_y}$ are the input voltages to the PMAs, and $u_k(t) \in \mathbb{R}^{n_u}$ are the measured outputs. The operator $K(p(t))$ corresponds to $K(p(t)): u_k \mapsto y_k$

and it is expressed with the notation

$$K(p(t)) = \left[\begin{array}{c|c} A_k(p(t)) & B_k(p(t)) \\ \hline C_k(p(t)) & D_k(p(t)) \end{array}\right]. \tag{7}$$

For a frozen (constant) scheduling value $p(t) \equiv p \in \mathcal{P} \subset \mathbb{P}$, $K(p)$ defines an LTI system. The closed-loop map $T(G, K(p(t)))\colon d_i \mapsto y$, given by

$$T(G, K(p(t))) = (I + GK(p(t)))^{-1}G \tag{8}$$

is an LPV system comprised of the LTI plant subject to an LPV controller and varying disturbance. This separation will significantly simplify the developed toolchain as will be shown in the sequel.

The control problem is schematically shown in Fig. 1(b), where G is the LTI system, $K(p(t))$ is the LPV controller, and d_i represents the microvibration disturbances. In terms of control objectives, the following typical requirements have to be satisfied for all $\Omega(t) \in \mathbf{\Omega}$.

R1: The closed-loop system in Fig. 1(b) is internally stable.

R2: To avoid excessive actuator degradation, the amplitude of the control signals must be kept below the physical limit of $u_{\max} = 10$ units and the frequency content must be limited to the bandwidth region. In addition, the disturbance attenuation factor of the closed-loop system needs to be pushed below a target value $\epsilon_{\max} = -20$ dB, i.e., microvibration disturbances should be reduced by a factor 10 through the active vibration isolation platform. The factor $\epsilon_{\max}$ is chosen to safely attenuate disturbances without saturating the PMAs.

R3: The controller must be of low-complexity such that implementation is feasible with limited computational resources.

Here, low-complexity refers to the complexity of the controller in terms of the state dimension and scheduling dependency structure. This is further elaborated upon in Section IV-C. To verify the performance of the controller, the following metrics are analyzed a posteriori. We define the reduction ratio as follows:

$$\rho = 1 - \frac{\|y_{\mathrm{CL}}\|_{\mathrm{rms}}}{\|y_{\mathrm{OL}}\|_{\mathrm{rms}}} \tag{9}$$

where $\|x\|_{\mathrm{rms}} = ((1/N)\sum_{n=1}^{N} x[n]^2)^{1/2}$ denotes the *root mean squared* (rms) norm, with $x[n]$ the nth element of the vector $x \in \mathbb{R}^N$, y_{OL} is the measured response without compensation and y_{CL} is the measured system response with compensation. The reduction ratio indicates the percentage of how much the disturbance is suppressed in the plant response. Furthermore, we define the disturbance rejection factor for a constant disturbance frequency $\bar{\Omega}$ by

$$r_{\bar{\Omega}} = |Y_{\mathrm{OL}}(\bar{\Omega})| - |Y_{\mathrm{CL}}(\bar{\Omega})|. \tag{10}$$

The disturbance rejection factor indicates the reduction magnitude of the frequency spectrum $Y(\bar{\Omega})$ as a result of closing the loop, i.e., how much disturbance rejection is obtained.

In Section III, the proposed identification methodology is presented, after which the control design procedure is discussed in Section IV.

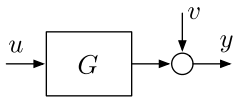

Fig. 3. Schematic of the data generating system used for FRF estimation.

III. System Identification of the Test Platform

A. Identification Setup

In this section, we propose an identification methodology for systems subject to frequency-varying disturbances. This constitutes to Contribution C2. The goal is to obtain a model of the system, i.e., from the actuator to the point-of-interest, describing $G\colon u \mapsto y$. In this framework, we consider the frequency-varying microvibration disturbances to be generated by an LPV filter, while the underlying model of the plant remains LTI. Hence, only an LTI model of the plant is to be identified, which significantly simplifies the identification.

Although in space applications, the microvibration disturbances are forces and torques generated mostly by the ACSs, in our study these are mimicked by input disturbances generated on the PMAs. Hence, the identification objective simplifies to identifying the lumped system $G = G_{\mathrm{ap}}G_{\mathrm{pma}}$ in Fig. 1(b). Furthermore, as the system G is assumed to be stable, we propose open-loop identification experiments. Hence, consider the data generating system depicted in Fig. 3, where G is the multivariable LTI system, u is the excitation signal applied to the PMAs, which will be specifically designed for identification in Section III-B3. The signal y is the observation of the plant output, polluted by v, corresponding to measurement noise and other stochastic disturbances. We propose to first estimate a *frequency response function* (FRF), which is an MIMO nonparametric model of the underlying electromechanical transfer to the point of interest. This is followed by fitting a multivariable parametric model on the nonparametric FRF estimate.

B. Nonparametric FRF Estimation

1) Estimation Concept: FRFs allow for intuitive visual insight in system characteristics including compliance, parasitic dynamics, and information on locations and properties of flexible mode shapes [23], [24]. There are a variety of algorithms available to obtain an FRF estimate. Commonly used algorithms apply the spectral analysis method, see [25]. Considering the data generating system in Fig. 3, the measured system response to an excitation signal u is related in the frequency domain by

$$Y(k) = G(i\omega_k)U(k) + V(k) + R(k) \tag{11}$$

where $G(i\omega_k) \in \mathbb{C}^{n_y \times n_u}$ is the transfer function matrix of the data generating system, $Y(k) \in \mathbb{C}^{n_y}$ is the noisy output spectrum, $U(k) \in \mathbb{C}^{n_u}$ is the input spectrum, $V(k) \in \mathbb{C}^{n_y}$ is the spectrum of the noise signal, and $R(k) \in \mathbb{C}^{n_y}$ is the lumped transient and leakage term, with k the frequency index and $\omega_k \in \mathcal{F} = \{\omega_k\}_{k=1}^{N_f}$ are the frequencies corresponding to the frequency bins associated with the *discrete Fourier transform* (DTF) of the measured signals. Furthermore, we denote $i = \sqrt{-1}$. The transient and leakage term $R(k)$ together with

the noise $V(k)$ pollutes the frequency content of $Y(k)$. Since the IO relationship (11) has n_y equations with $n_y n_u$ unknowns, $G(i\omega_k)$ cannot be identified from a single experiment. Hence, we require at least n_u experiments with different excitation signals. Consequently, the empirical transfer function estimate is obtained as follows:

$$\hat{G}(i\omega_k) = \bar{Y}(k)\bar{U}^{-1}(k) \tag{12}$$

with $\bar{U}(k) = \begin{bmatrix} U_1(k) & \cdots & U_{n_u}(k) \end{bmatrix} \in \mathbb{C}^{n_u \times n_u}$ and $\bar{Y}(k) = \begin{bmatrix} Y_1(k) & \cdots & Y_{n_u}(k) \end{bmatrix} \in \mathbb{C}^{n_y \times n_u}$. Here, the ith column of $\bar{U}(k)$ and $\bar{Y}(k)$ corresponds to an experiment with input signal $U_i(k)$ and output signal $Y_i(k)$. It is clear that solving (12) puts a strong condition on the design of the excitation signal, where $\bar{U}(k)$ should be nonsingular for each k. The design of this excitation signal is further discussed in Section III-B3.

Furthermore, note that the FRF estimate (12) is corrupted by transient terms $R(k)\bar{U}^{-1}(k)$ in addition to the effect of the noise $V(k)$. For periodic input signals, the bias due to leakage errors is 0 at the harmonics of the input signal. Moreover, multiple periods and realizations can be measured and subsequently averaged to reduce the effects of noise. For nonperiodic signals, the leakage errors can be suppressed by applying a smoothing operation; however, these smoothing operations can easily introduce bias in the estimates [26].

2) FRF Estimation by LPM: To suppress aforementioned leakage errors we propose to use the *local polynomial method* (LPM), see [26]. The main advantage of the LPM is in the suppression of the leakage errors $R(k)$ in (11). The idea behind the LPM is to exploit the smoothness of the FRF and transient terms to locally approximate them at the DFT bins ω_k by a (low order) polynomial. In that sense, for all ω_k, a local parametric model of the FRF G_0 and the transient term R is estimated in polynomial form in a narrowband around each DFT frequency ω_k. Then, the central value of the polynomial is used as an estimate of $G_0(i\omega_k)$. Consequently, the transient effects are removed from the output spectrum in (11) to obtain the sample mean $\hat{Y}(k)$, effectively eliminating them. This is the main reason to prefer the LPM over regular empirical transfer function estimation methods. The design of the excitation $U(k)$ is discussed next.

3) Experimental Design: A white noise excitation signal is often used for identification because of its ease of use, but consequently introduces leakage errors that degrade the FRF quality [26]. This motivates the use of periodic excitation signals, which reduce leakage effects and enable to define the spectrum of the excitation on a user-specified frequency grid $\mathcal{F}$.

To satisfy the identifiability conditions for (12), we require a nonsingular input matrix $\bar{U}(k)$. This is achieved by designing one scalar multisine $u_{\text{ms}}(t)$ that excites all frequencies of interest. Next, n_u independent excitation signals are obtained by multiplying the spectrum $U_{\text{ms}}(k) \in \mathbb{C}$ with an orthogonal matrix $\tilde{T} \in \mathbb{C}^{n_u \times n_u}$, often taken as a Hadamard matrix, resulting in the excitation signal

$$\bar{U}(k) = U_{\text{ms}}(k)\tilde{T} \tag{13}$$

where ith column of $\bar{U}(k)$ refers to the DFT spectrum of an n_u dimensional vectorial excitation signal for the ith experiment.

For the considered setup, the multisine is defined by

$$u_{\text{ms}}(t) = \sum_{k \in \mathcal{F}} A_k \cos(\omega_k t + \phi_k) \tag{14}$$

on the frequency grid $\omega_k \in \mathcal{F}$, where $\mathcal{F} = \{2\pi 0.1k\}_{k=1}^{N_f}$ is chosen, with amplitudes A_k, and random phases ϕ_k. For the considered application, every A_k is chosen the same such that: 1) the excitation signal remains within actuator saturation limits and 2) the excitation signal remains within the linear range of the PMAs. The phases ϕ_k are randomized such that $\bar{U}(k)$ is orthogonal. Regarding the test setup, due to the nonlinear effects of the PMAs for large voltages, an individual design of $U(k)$ is pursued. Specifically, every PMA is excited individually, i.e., $\tilde{T} = I$. We recommend to use multiple periods of the excitation signal to reduce the effects of noise on the FRF estimate. Here, we use 20 multisine periods of which the first 2 are removed to eliminate transient effects.

4) Estimation Results: The results of the nonparametric FRF identification on the vibration isolation test setup are depicted in Fig. 4. The confidence bounds are calculated from the noise co-variance matrix of the FRF, where the width of the $a \cdot 100\%$-confidence interval of element (i, j) of the FRF matrix is calculated as follows:

$$R_{i,j}(k) = \sqrt{-\ln(1-a)}\sqrt{\sigma^2_{i,j}(k)} \tag{15}$$

where $\sigma^2(k)$ is the plant co-variance [26, Chapter 2.4.2].

It can be observed that at frequencies where the magnitude of the FRF is low, the uncertainty interval in terms of the confidence bounds grows. This makes sense, as in these regions the SNR is small. In the regions where the FRF magnitude is the largest, the confidence interval is narrow. In these regions, the PMAs have authority such that disturbance suppression can take place. Since the plant is estimated accurately in the frequency regions of control authority, the nonparametric system identification is considered successful.

C. Parametric TF Fitting

In this section, we fit a parametric model on the estimated FRF data. The goal is to find an MIMO LTI model $\breve{G}(s, \theta)$ of fixed order, parameterized in the real-valued parameter vector θ, which approximates the FRF data $\hat{G}(i\omega)$. This model is represented by a left polynomial matrix fraction description

$$\breve{G}(s, \theta) = A^{-1}(s, \theta)B(s, \theta) \tag{16}$$

where A is a monic polynomial and B is a polynomial matrix in s, each parameterized linearly by θ. The approximation of the FRF data by the model is characterized by the additive error

$$E(i\omega_k, \theta) := W(i\omega_k) \odot \left(\hat{G}(i\omega_k) - \breve{G}(i\omega_k, \theta)\right) \tag{17}$$

with $W(i\omega)$ a weighting filter used to specify a weighting on a user-relevant region of interest and $\odot$ denotes the elementwise product. The goal of the procedure is to find an estimate of the parameter θ that minimizes

$$\hat{\theta} = \arg\min_{\theta \in \mathbb{R}} J(\theta) \tag{18}$$

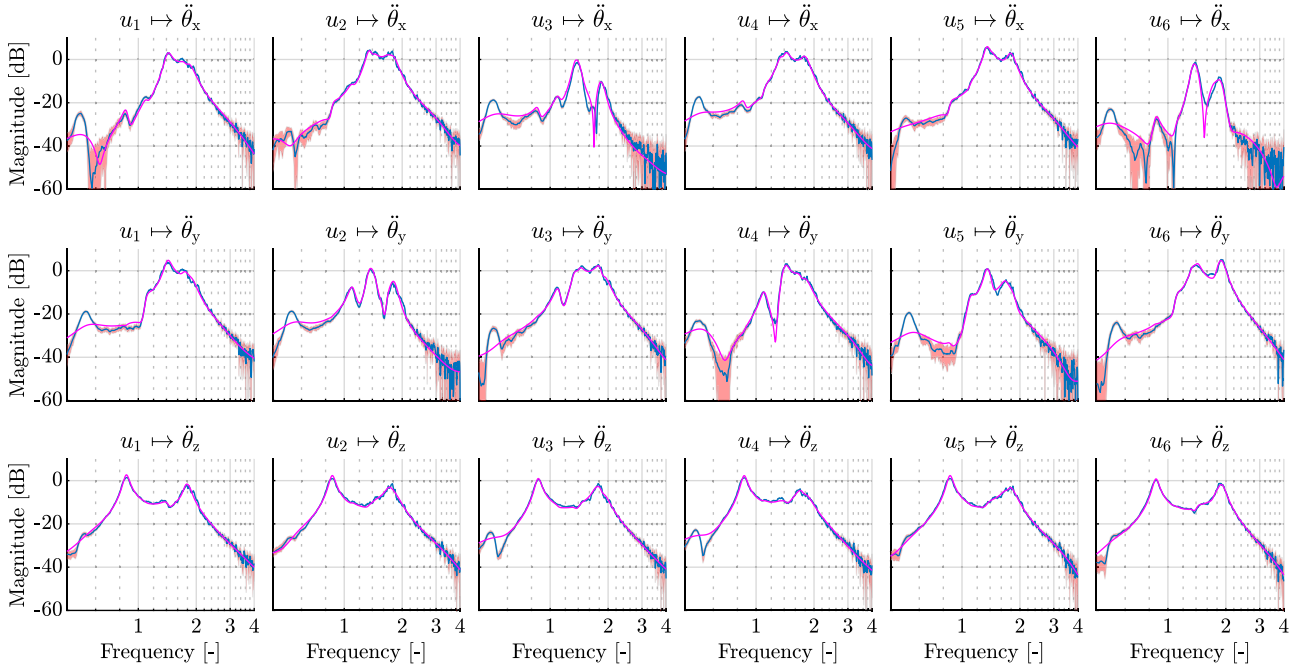

Fig. 4. Identification results of the vibration isolation setup. The blue line denotes the estimated FRF, the orange region depicts the corresponding 99% confidence bound, and the magenta curve describes the identified parametric model.

where the cost function is defined as follows:

$$J(\theta) := \|E(\theta)\|_F^2 = \sum_{k\in\mathcal{F}} \mathrm{tr}\big(E(i\omega_k,\theta)E^*(i\omega_k,\theta)\big) \quad (19)$$

where tr(.) denotes the trace of a matrix and $*$ is the complex conjugate transpose, giving that the right-hand side of (19) corresponds to the Frobenius norm of $E(i\omega_k,\theta)$. To solve (19), the algorithm in [27] is employed.

For the considered setup, based on the estimated FRFs, a left polynomial matrix fraction description of order 36 is estimated. Because of the one-to-one correspondence between matrix fraction descriptions and state-space models, this leads to a state-space model with low McMillan degree [28]. The Bode magnitude plots are shown in Fig. 4. Visually, satisfactory results are obtained without weighting filters. To quantify the goodness of the estimate, the following metric is defined

$$\Delta_m = \max_{\omega\in\mathcal{F}} \bar{\sigma}\left(\breve{G}(i\omega_k) - \hat{G}(i\omega)\right) \quad (20)$$

where $\bar{\sigma}$ denotes the maximum singular value. The above metric connects the identification criterion (19) to a robust control-relevant identification metric, see [28]. Here, a low value indicates a small uncertainty set, hence accurate identification. The achieved value $\Delta_m = 0.5438$ indicates that the fit accuracy is good. This is confirmed by inspection of the maximum singular values of $\hat{G}$ and $\breve{G}$ over frequencies in Fig. 5. It shows that the dominant behavior of the system is captured accurately by the model, especially in the mid-to-high-frequency ranges where the disturbance is dominant, which is also the control-relevant frequency region. Hereby, the parametric identification is considered successfully.

IV. Control Design

In this section, the proposed control design procedure is discussed. The challenge is to design the LPV controller

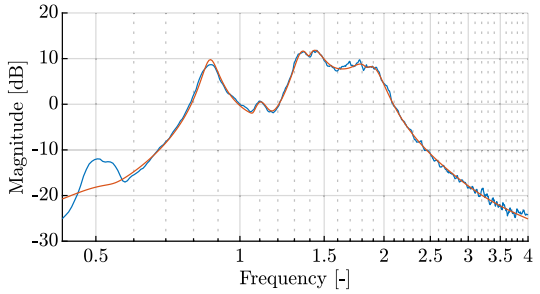

Fig. 5. Bode magnitude plot of the maximum singular value of the estimated MIMO FRF (blue) and the identified parametric model (orange). This confirms that the dominant behavior of the system is captured accurately.

$K(p(t))$ with $p = \Omega$ such that Requirements R1–R3 are met for all considered main harmonics $\Omega(t) \in \mathbf{\Omega}$. In order to design the control law, the synthesis problem is cast into the $\mathcal{H}_\infty/\mu$ framework [20]. This section corresponds to C1.

A. Control Architecture

With the available IO partition, a nonsquare plant model has to be used for synthesis, which results in a nonsquare controller. Since the model cannot be reduced to lower order without introducing significant model error, standard synthesis techniques are not applicable as they result in controllers with state dimensions that are too large ($\geq$56) to comply with Requirement R3. Hence, to accommodate Requirement R3, a structured control design of limited complexity is proposed. The selected structure of the controller is further discussed in Section IV-C2.

The considered control architecture is given in Fig. 1(b), which is recasted into the well-known generalized plant formulation in Fig. 6. By Requirement R2, we aim at attenuating the microvibration disturbances by a factor $\epsilon_{\max}$. Since microvibration disturbances occur on the input of the

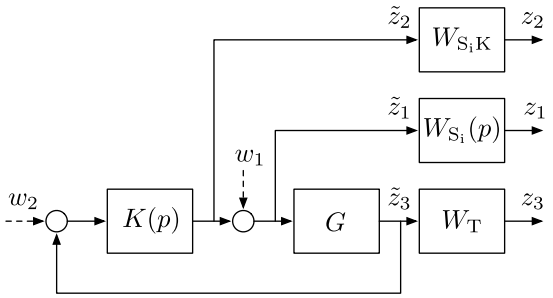

Fig. 6. Weighted synthesis model for MIMO controller design for the microvibration isolation setup.

PMAs, it is beneficial to achieve a small input sensitivity $w_1 \mapsto \tilde{z}_1 : S_i = (I + K(p)G)^{-1}$ at the disturbance frequencies. Note that frequency response of S_i is understood in the frozen sense, i.e., $p(t) \equiv p \in \mathbb{P}$, and the disturbance frequencies are dependent on p. A small input sensitivity at the disturbance frequencies implies that the microvibrations are attenuated by the closed loop, thus achieving disturbance rejection. Next to disturbance rejection, it is important to limit the control signal and sensor noise amplification by weighting the control sensitivity $w_2 \mapsto \tilde{z}_2 \colon S_i K(p)$ and complementary sensitivity $w_2 \mapsto \tilde{z}_3 \colon T = G S_i K(p)$, respectively. To shape these sensitivities, weighting filters $W_\bullet$ are introduced such that $W_{S_i} S_i \colon w_1 \mapsto z_1$, $W_{S_iK} S_i K(p) \colon w_2 \mapsto z_2$, and $W_T T \colon w_2 \mapsto z_3$ represent the weighted generalized performance channels.

B. Weighting Filter Design

The goal of this section is to explain how the weighting filters can be selected in a systematic way to capture the design Requirements R1 and R2. Because the microvibration disturbances enter on the input side of the system, the disturbance model derived in Section II-B directly relates to the design of the input sensitivity weighting filter W_{S_i}. The input sensitivity describes how the system reacts to disturbances in the input. An input sensitivity of one in a certain frequency band indicates that the system does not actively suppress disturbances, i.e., the system relies on the passive isolators to reject disturbances. Ideally, the input sensitivity is small in the frequency ranges, where the disturbances occur to provide additional suppression of the microvibrations.

To model the varying spectral components of a single harmonic of the disturbance (1) in terms of a weighting filter, consider the following LPV filter

$$N_i(p(t)) = \left[\begin{array}{cc|c} 0 & 2\pi h_i p(t) & 0 \\ -2\pi h_i p(t) & -2\beta h_i p(t) & p(t) \\ \hline 0 & 2\beta h_i p(t)(\varsigma - 1) & 1 \end{array}\right]. \quad (21)$$

Here, $\beta = 0.005$ defines damping around the varying central frequency $p(t) = \Omega(t)$. A lower value indicates less damping, i.e., the peak of the notch filter is sharper and narrower. Alternatively, a larger value can be used to compensate disturbances in a larger frequency band. The value ς indicates the amount of disturbance attenuation. If multiple harmonics are considered, multiple filters N_i for different harmonic numbers h_i can be connected in series. Ideally, we tune the control system to achieve maximum isolation performance. However, the isolation performance is limited by the signal-to-noise ratio and the actuator constraints, hence we aim for $\epsilon_{\max} = 20$ dB attenuation. This results in the following input sensitivity weighting filter structure

$$W_{S_i}(p(t)) = M_{S_i} \mathrm{diag}\left(\prod_{i=1}^{N_d} N_i(p(t)) I_{n_u}\right) \quad (22)$$

where I_{n_u} is the $n_u \times n_u$ identity matrix and M_{S_i} is used to set an upper bound magnitude of the input disturbance. For the considered setup, the disturbance is only introduced on PMA 2; hence, only the (2, 2) element of the input sensitivity weighting filter needs to contain this inverse notch structure. This results in an input sensitivity weighting filter

$$W_{S_i}(p(t)) = M_{S_i} \mathrm{diag}\left(1, \prod_{i=1}^{N_d} N_i(p(t)), 1, 1, 1, 1\right) \quad (23)$$

where $M_{S_i} = 0.5$. The broadband noise component d_{bn} in (1) is neglected as the noise level is much smaller than the noise of the acceleration sensors. The (2, 2) element of W_{S_i} for $N_d = 1$ is displayed in Fig. 7.

The control sensitivity weight W_{S_iK} is used to limit the control action to the actuator specifications, to introduce a roll-off action outside the disturbance bandwidth in order to reduce the effects of noise, and to limit the frequency content of the actuators. This results in the following control sensitivity weighting filter structure

$$W_{S_iK} = u_{\max}^{-1} \frac{(s + 2\pi f_{\mathrm{lp}})^2}{\left(\frac{1}{\alpha} s + 2\pi f_{\mathrm{lp}}\right)^2} I_{n_u} \quad (24)$$

where we consider $u_{\max} = 10$ to limit the control action, $f_{\mathrm{lp}} = 1.07$ introduces a low-pass action outside the frequency-range of interest, and $\alpha = 20$ is used to ensure a biproper weighting filter.

Similarly, the complementary sensitivity weight W_T is designed to suppress measurement noise outside the bandwidth region

$$W_T = \frac{1}{\sqrt{2}} \frac{(s + 2\pi f_{\mathrm{lp}})^2}{\left(\frac{1}{\alpha} s + 2\pi f_{\mathrm{lp}}\right)^2} I_{n_y}. \quad (25)$$

The weighting filters W_{S_iK} and W_T are given in Fig. 7.

C. LPV Controller Synthesis

1) General Concept: With the weighting filters $W_\bullet$, the generalized plant in Fig. 6 is constructed. Hereby, the optimization criterion

$$\min_K \max_{p \in \mathbf{\Omega}} \left\| \begin{bmatrix} W_{S_i} S_i & 0 & 0 \\ 0 & W_{S_iK} S_i K & 0 \\ 0 & 0 & W_T T \end{bmatrix} \right\|_{\mathcal{L}_2} < \gamma \quad (26)$$

defines the synthesis of a stabilizing MIMO LPV controller K. As assumed in Section II-B, we consider that the rate of change $|\dot{\Omega}(t)| \leq 0.01$ is significantly slower than the frequency range, in which the disturbances are active, i.e., $p(t) \in \mathbb{P} = [0.59, 1.07]$. This motivates the use of local LPV approaches. Accordingly, under a parameterized form of the LPV controller (6), (26) can be optimally solved for fixed

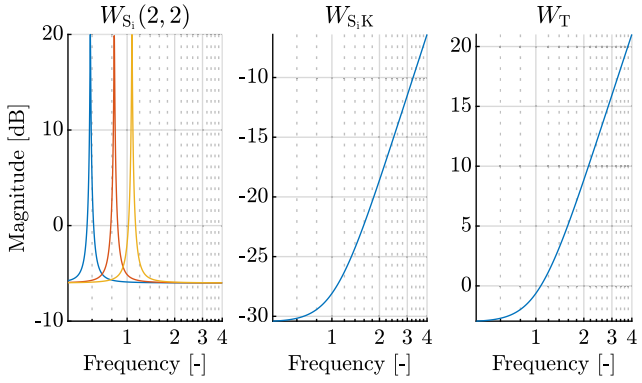

Fig. 7. Weighting filters used for controller synthesis. The left figure depicts the (2, 2) element of the LPV weight W_{S_i}, for frozen values $p(t) \equiv p \in \{0.59, 0.83, 1.07\}$. The middle figure depicts the diagonal element(s) of weight W_{S_iK}, while the right figure depicts the diagonal element(s) of weight W_T.

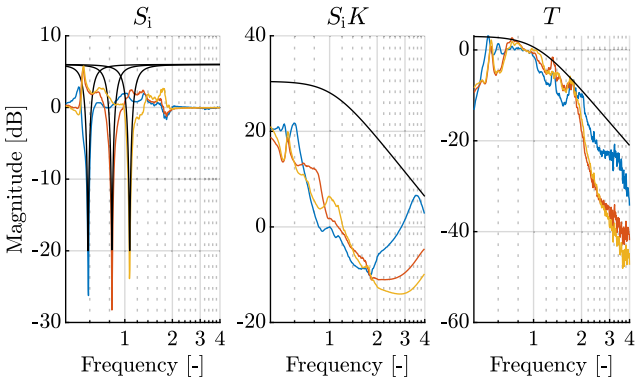

Fig. 8. Closed-loop sensitivity functions based on local frequency responses of the controller $K(p)$ and the estimated FRF data as the plant. In the left subfigure, the second diagonal element of the input sensitivity function is depicted. The middle and right subfigures show the dominant singular values of the control and complementary sensitivity functions over frequency. In blue, orange, and yellow the closed-loop local frequency responses are displayed for $p \in \{0.59, 0.83, 1.07\}$ with the inverse weighting filters in black. We can conclude that our performance objectives are satisfied and the controller contains sharp gains to combat the harmonic disturbances.

values of $p(t) \equiv p \subset \mathbb{P}$ in a gridded sense using $\mathcal{H}_\infty$ methods. To overcome the disadvantages of high-order controllers synthesized with typical model-based methods and to comply with the constraints of Requirement R3, non-smooth $\mathcal{H}_\infty$ tools are used to solve (26) and synthesize a low-order structured LPV controller that internally stabilizes the closed-loop system for all frozen p [29], [30]. To this end, the scheduling set $\mathbb{P}$ is represented by a parametric uncertainty set $\Delta_p = \{\delta I_{n_\Delta} \mid \delta \in [0.59, 1.07]\}$. As such, stability and performance guarantees are only guaranteed locally for frozen instances of $p(t)$, i.e., $p(t) \equiv p \in \Delta_p$, and for sufficiently slow time variations of $p(t)$ as shown in [31, Section 2.2]. Hence, given the slow variations of the microvibration disturbances, which are relatively small compared to the closed-loop dynamics, the time-varying aspects of p for stability are assumed to be minor and of no significant influence. This is further confirmed by the experimental results in Section V. The considered controller structure and parameterization are discussed next.

Remark 1: The control architecture used for synthesis is not standard. In (26), a diagonal weighting structure between the three considered sensitivities is sought. This can significantly improve the achieved performance compared with standard mixed-sensitivity or four-block shaping problems as each sensitivity is considered individually.

2) Controller Structure: To limit the computational demand of the active vibration isolation solution, a structured controller is proposed. To this end, consider the controller $K(p(t)) = \mathcal{F}_l(\hat{K}, \Delta_K(p(t)))$, with $\hat{K}$ and $\Delta_K(p(t))$ formulated as follows:

$$\hat{K} = \begin{pmatrix} A & B_w & B_u \\ C_z & D_{\text{zw}} & D_{\text{zu}} \\ C_y & D_{\text{yw}} & D_{\text{yu}} \end{pmatrix}, \quad \Delta_K(p(t)) = p(t) I_\Delta. \tag{27}$$

To reduce the computational complexity of the synthesis and implementation, $A \in \mathbb{R}^{n_x \times n_x}$ is restricted to be tridiagonal with state-order $n_x = 12$. To further reduce the computational complexity of the controller on the hardware, the matrix $D_{\text{zw}} \in \mathbb{R}^{n_\Delta \times n_\Delta}$ is set to be 0 such that affine scheduling dependency is enforced. Moreover, D_{yu} and D_{zu} are set to 0 to enforce a strictly proper controller, and n_Δ is set to 6. The affine scheduling dependency allows the controller to reschedule for a measured spin rate $p(t)$ and complements the affine scheduling dependency structure of the weighting filter W_{S_i}. The achieved results are shown in Fig. 8 and are elaborated upon in Section V.

D. Discretization

In this section, we show how to apply a Tustin discretization method that matches the local resonance modes of the CT LPV controller with the DT LPV controller. A common method to discretize controllers containing resonance modes close to the Nyquist frequency is Tustin discretization [32]. This results in the DT controller $K_{\text{DT}}(p(nT_s))$

$$\begin{bmatrix} x_k(n+1) \\ z_k(n) \\ y_k(n) \end{bmatrix} = \mathcal{B} \star \mathcal{F}_l\big(\hat{K}, \Delta_K(nT_s)\big) \begin{bmatrix} x_k(n) \\ w_k(n) \\ u_k(n) \end{bmatrix} \tag{28}$$

where $n \in \mathbb{N}$ is the sampling instant and the matrix $\mathcal{B}$ defines the Tustin transformation

$$\mathcal{B} = \begin{bmatrix} I_{n_x} & \tau I_{n_x} \\ I_{n_x} & \dfrac{\tau}{2} I_{n_x} \end{bmatrix} \tag{29}$$

where $\tau = T_s$ is typically chosen to be equal to the sampling time [33], see also [34] for criteria to choose appropriate sampling times for discretization of LPV systems. Consequently, low-frequency dynamics are mapped accurately in the frequency domain, whereas for frequencies approaching the sampling frequency, the accuracy deteriorates. In the context of this application, the relatively high bandwidth combined with the low sampling time makes it difficult to accurately discretize the controller. This is especially detrimental for the considered controller with inverse notch structures that require to be accurately represented. To improve the discretization accuracy at these frequencies, a frequency prewarp transformation

$$\tau = \frac{2\tan(0.5\omega_p T_s)}{\omega_p} \tag{30}$$

can be included, which ensures the matching of the continuous and discrete frequency response at the frequency ω_p. Note that a frequency prewarp can only improve the fit at a single frequency point of interest, while outside of this point, the discretization distortions remain.

However, in the LPV setting where the disturbance frequency varies over time, the frequency prewarp point of interest ω_p should also change along with $p(t)$. Therefore, to increase the discretization fit and performance of the DT controller, we consider scheduling the frequency prewarp parameter τ in relation to the disturbance scheduling p, i.e.,

$$\tau(p(nT_s)) = \frac{2\tan(0.5\ p(nT_s)T_s)}{p(nT_s)}. \tag{31}$$

This implies that the original scheduling block Δ_K extends to

$$\Delta_{K,e}(p(nT_s)) = \mathrm{diag}(\Delta_K(nT_s), \tau(p(nT_s))I_{n_x})). \tag{32}$$

As such, the scheduling dependency of the DT controller increases with the state dimension of the CT controller.

Remark 2: For implementation on hardware, the star product in (28) can be precomputed and absorbed in the controller matrices. Implementation of the DT controller then amounts to the evaluation of the scheduling-dependent controller matrices at every sampling instant when the scheduling variable changes, i.e., when $p(nT_s) \neq p((n-1)T_s)$.

Remark 3: When multiple harmonics are considered, each harmonic structure in the controller can be discretized individually by the proposed discretization methodology. This can be achieved by decomposing the controller structure into individual modes, followed by individual discretization of the inverse notch components.

E. Stability Analysis

As during the controller design, a parametric model of the plant was fit on the estimated FRF $\hat{G}$, it is important to verify stability of the LPV controller in closed loop with the complete model dynamics before implementation on the hardware. Therefore, we propose an a priori stability test based on the generalized CT MIMO Nyquist stability theorem, see [35, Chapter 4.9]. To evaluate the closed-loop stability along the scheduling trajectory $p(t)$, Nyquist stability is assessed for a dense grid of frozen operating points $p(t) \equiv p \in \mathcal{P}$.

Theorem 1 (MIMO Nyquist Theorem): Let P_{ol} be the number of open-loop unstable poles in $L(p) = GK(p)$. The closed-loop system with loop transfer function $L(p)$ and negative feedback is stable if and only if the Nyquist plot of $\det(I + L(p))$ along the D-contour.[2]

1) Makes P_{ol} anticlockwise encirclements of the origin.
2) Does not pass through the through the origin.

We refer to [35, Chapter 4.9] for more details. The Nyquist test allows for the use of the FRF data $\hat{G}(i\omega)$ of the identified plant. This avoids possible modeling errors that are built up throughout the parametric modeling procedure.

For a frozen $p \in \mathcal{P}$, the CT loop transfer is given by

$$L(p, i\omega) = \hat{G}(i\omega)K(p, i\omega) \tag{33}$$

[2]A clockwise contour which contains the imaginary axis and encloses the right half of the complex plane.

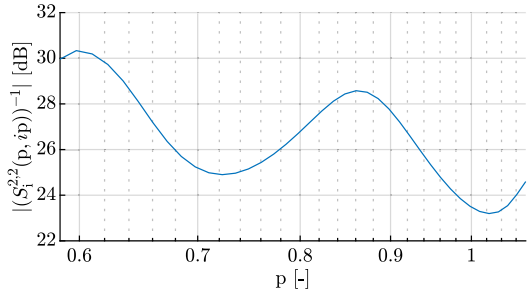

Fig. 9. Expected disturbance rejection level over the scheduling envelope $p \in \mathbb{P}$. The expected disturbance attenuation factor satisfies Requirement R2 in the frozen sense for the considered scheduling envelope.

where $K(p, i\omega)$ is the frequency response (Fourier transform) of the controller, see [36, Chapter 10].

To assess closed-loop stability, the Nyquist stability test is performed for a dense scheduling grid $p \in \mathcal{P}$. Therefore, conclusions can only be drawn on local stability at the frozen operating points $p \in \mathcal{P}$. However, since $\dot{p}$ is assumed to vary slowly, adhering to the Nyquist stability criterion on a dense grid can qualify as a valid a priori stability test for the interconnection between the plant and LPV controller.

V. Experimental Results

A. Frequency-Domain Analysis

The achieved analytic closed-loop behavior under the considered weighting filters are shown in Fig. 8. A performance criterion of $\gamma = 0.9129 < 1$ is achieved, which indicates a successful design. The left subfigure shows that the disturbance rejection goal of 20 dB is achieved for frozen rotational velocities generated main harmonics p. The evaluation of the expected disturbance rejection level over the considered frequency envelope is depicted in Fig. 9. Based on this figure, we can conclude that the expected 20-dB disturbance attenuation is achieved. Furthermore, the middle subfigure of Fig. 8 shows that, under the considered disturbance specifications, the control signal will remain within 10 and rolls of by at least -40 dB/dec, with a cutoff frequency of 1.07. In the right subfigure, the complementary sensitivity function shows that measurement noise is not amplified above the control bandwidth frequency of 1.07. Hereby, all design goals are met. Next, the performance of the implemented controller on the experimental setup is evaluated.

B. Local Experiments

To assess the performance of the controller, first local experiments with frozen harmonic frequencies, i.e., $\Omega(t) \equiv \bar{\Omega} \in \mathcal{P} = \{0.59, 0.83, 1.07\}$, and with a single harmonic component, i.e., $N_d = 1$, are conducted. Here, the plant is disturbed by harmonic disturbances (2) with constant frequencies $\Omega(t) \equiv \bar{\Omega} \in \mathcal{P}$. Concurrently, the plant response is measured both in open loop and closed loop. In this setting, the frozen experiments are used to measure disturbance suppression at each $\bar{\Omega}$. Because the setup is significantly less compliant in the θ_x- and θ_y-directions, a relatively large input disturbance amplitude, $A_1 = 4$ in (2), is applied over the PMAs in order to measure the disturbance effect on the output.

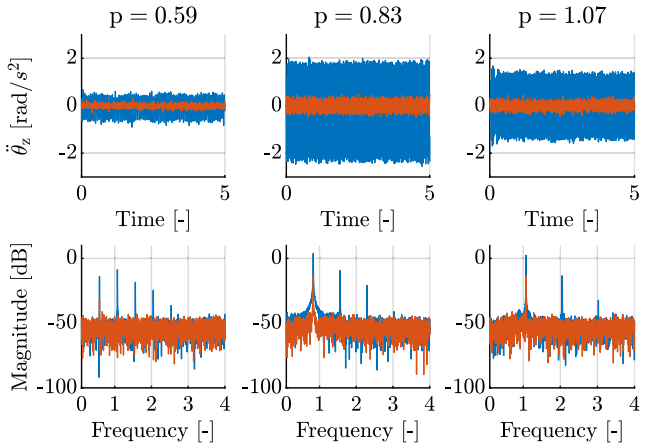

Fig. 10. Experimental results of the MIMO LPV controller evaluated at the θ_z-axis for frozen disturbances. The left two subfigures denote, from top to bottom, the open- (blue) and closed-loop (orange) plant response and frequency spectrum for disturbances $p = 0.59$. The middle and right two subfigures contain the same measurements for $p = 0.83$ and $p = 1.07$, respectively. The time-domain plots indicate that high disturbance rejection is, indeed, achieved by the designed controller. The frequency spectra show rejection of the main harmonic and also display the PMA nonlinearities.

Due to nonlinearities in the PMAs, this results in integer multiples of the main harmonics.

The results of these experiments are summarized in Fig. 10. For brevity, we only show the measurement results on the θ_z-axis. The results for the other axes are similar. In the time-domain plots, we see a significant reduction in the output vibration; hence, the vibration disturbances are actively suppressed. The reduction ratios are given in Table I, which confirms this observation.

From the frequency spectra, the magnitudes of disturbance suppression for $\bar{\Omega} \in \mathcal{P}$ are lower than expected. This is also confirmed by the disturbance rejection factors in Table I. This is partly due to the controller discretization, the discrepancy between the system and the model, noise, and nonlinear effects. Furthermore, in Fig. 10, we can clearly see the nonlinear effects of the disturbance, where integer multiples of the main harmonic component are observed. However, when the main harmonic is only partly suppressed, the nonlinear (integer multiples of the main harmonic) effects are also attenuated. This happens because the PMA control signals that attenuate the disturbances are also subject to the same nonlinear PMA dynamics, hence rejecting integer multiples of the main harmonic. This also confirms that the nonlinear dynamics are not relevant in evaluating the performance of the controller.

C. Experiments With Space-Realistic Scheduling Trajectories

Next, the performance of the controller is evaluated for disturbance signals with varying frequencies according to $\Omega(t) \in \mathbf{\Omega}$ and $|\dot{\Omega}(t)| \leq 0.01$. To reduce experiment time, the microvibration disturbances are limited to the frequency region $\Omega(t) \in [1.00, 1.07]$. This experiment allows to determine whether the rate of change of the disturbance frequency poses a limiting factor to performance. The results are shown in Fig. 11. From the time-domain plot, we observe a significant suppression of the disturbance. This is also confirmed by

TABLE I

REDUCTION RATIOS AND DISTURBANCE REJECTION FACTORS [DEFINED BY (9) AND (10)] FOR EXPERIMENTS WITH FROZEN DISTURBANCE FREQUENCIES. $\rho_{\bar{\Omega}}$ AND $r_{\bar{\Omega}}$ INDICATE THE REDUCTION RATIO AND DISTURBANCE REJECTION FACTORS FOR THE SINUSOIDAL DISTURBANCE WITH CONSTANT FREQUENCY $\bar{\Omega}$. A SIGNIFICANT REDUCTION IN MICRVIBRATION DISTURBANCES IS OBSERVED

	$\rho_{0.59}$	$\rho_{0.83}$	$\rho_{1.07}$	$r_{0.59}$	$r_{0.83}$	$r_{1.07}$
θ_x	63.11	87.73	83.95	13.26	21.24	23.63
θ_y	65.69	71.74	84.68	20.58	19.05	19.55
θ_z	65.64	85.22	82.13	17.02	17.05	15.93

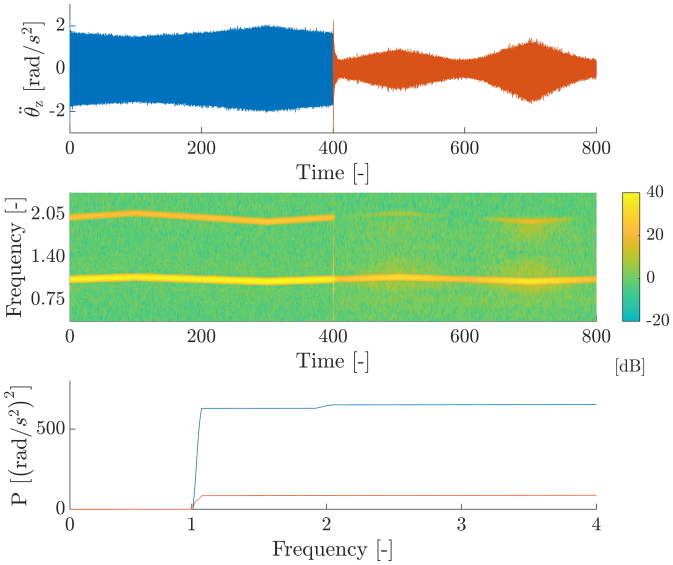

Fig. 11. Experimental results of the MIMO LPV controller, rejecting varying disturbance frequencies for the θ_z-axis. The top figure depicts the acceleration measurement $\ddot{\theta}_z$ during the experiment. The middle figure shows the spectrogram of the plant response, generated using a short-time Fourier transform with a measurement length of 2 s. In the bottom figure, the cumulative power spectrum of the plant response is displayed. Significant microvibration reduction is achieved by the controller even when the disturbance frequencies vary.

TABLE II

REDUCTION RATIOS AND DISTURBANCE REJECTION FACTORS [DEFINED BY (9) AND (10)] FOR EXPERIMENTS WITH SPACE-REALISTIC VARYING DISTURBANCES FREQUENCIES. ρ IS THE REDUCTION RATIO AND r_{cps} IS THE DISTURBANCE REJECTION FACTOR BETWEEN THE CUMULATIVE POWER SPECTRA. A SIGNIFICANT REDUCTION IN MICROVIBRATION DISTURBANCES IS OBSERVED

	ρ	r_{cps}	$\|y_{\text{OL}}\|_{\text{RMS}}$	$\|y_{\text{CL}}\|_{\text{RMS}}$
θ_x	69.21	22.43	$6.347 \cdot 10^{-1}$	$1.954 \cdot 10^{-1}$
θ_y	69.01	22.06	$6.235 \cdot 10^{-1}$	$1.932 \cdot 10^{-1}$
θ_z	59.79	17.40	$1.121 \cdot 10^{0}$	$4.508 \cdot 10^{-1}$

the reduction ratios ρ in Table II. From the spectrogram, we can observe that the attenuation level of the disturbance is slightly less than expected based on Fig. 9, but results in near cancellation of the second PMA harmonic nonlinearity. The cumulative power spectra confirm these observations, where we observe a significant reduction in signal power, as also confirmed by the reduction ratios in Table II. The implementation results and analysis presented in this section form Contribution C2.

VI. Conclusion

In this work, we have proposed a complete design approach for active vibration isolation based rejection of frequency-varying harmonic microvibration disturbances for satellites where the main harmonic frequency is known. The process involves multisine-based MIMO frequency response identification of the mechanical behavior of the isolator and the payload together with an LPV disturbance modeling and control design methodology for actively rejecting microvibration disturbances. In the approach, the scheduling is based on the main harmonic frequency of a vibration disturbance, but, by introducing additional scheduling variables, the approach can be extended to multiple spectral components of incoming vibrations. Based on experimental results, we have successfully demonstrated that the proposed methodology is capable of nearly 60% reduction of microvibrations exerted on a prototype system, which gives promising outlooks for the deployment of the method in real missions.

References

[1] V. Preda, "Robust microvibration control and worst-case analysis for high pointing stability space missions," Ph.D. dissertation, IMS Lab., Bordeaux, France, 2017.

[2] C. F. Lillie, R. S. Polidan, and D. R. Dailey, "Key enabling technologies for the next generation of space telescopes," *Proc. SPIE*, vol. 7731, Jul. 2010, Art. no. 773102.

[3] C. Liu, X. Jing, S. Daley, and F. Li, "Recent advances in micro-vibration isolation," *Mech. Syst. Signal Process.*, vols. 56–57, pp. 55–80, May 2015.

[4] R. A. Masterson, "Development and validation of empirical and analytical reaction wheel disturbance models," Ph.D. dissertation, Massachusetts Inst. Technol., Cambridge, MA, USA, 1999.

[5] M. Le, "Micro-disturbances in reaction wheels," Ph.D. dissertation, Dept. Appl. Phys. Sci. Educ., Eindhoven Univ. Technol., Eindhoven, The Netherlands, 2017.

[6] E. Rivin, "Passive vibration isolation," *Appl. Mech. Rev.*, vol. 57, no. 6, p. 31, 2004.

[7] L. P. Davis, D. R. Carter, and T. T. Hyde, "Second-generation hybrid D-strut," in *Proc. SPIE*, vol. 2445, pp. 161–175, May 1995.

[8] Q. Luo, D. Li, and J. Jiang, "Coupled dynamic analysis of a single gimbal control moment gyro cluster integrated with an isolation system," *J. Sound Vibrat.*, vol. 333, no. 2, pp. 345–363, Jan. 2014.

[9] D. Stewart, "A platform with six degrees of freedom," *Proc. Inst. Mech. Eng.*, vol. 180, no. 1, pp. 371–386, 1965.

[10] V. Preda, J. Cieslak, D. Henry, S. Bennani, and A. Falcoz, "Robust microvibration mitigation and pointing performance analysis for high stability spacecraft," *Int. J. Robust Nonlinear Control*, vol. 28, no. 18, pp. 5688–5716, Dec. 2018.

[11] M. Alma, J. J. Martinez, I. D. Landau, and G. Buche, "Design and tuning of reduced order H-Infinity feedforward compensators for active vibration control," *IEEE Trans. Control Syst. Technol.*, vol. 20, no. 2, pp. 554–561, Mar. 2012.

[12] I. D. Landau, M. Alma, J. J. Martinez, and G. Buche, "Adaptive suppression of multiple time-varying unknown vibrations using an inertial actuator," *IEEE Trans. Control Syst. Technol.*, vol. 19, no. 6, pp. 1327–1338, Nov. 2011.

[13] J. S. Shamma and M. Athans, "Analysis of gain scheduled control for nonlinear plants," *IEEE Trans. Autom. Control*, vol. 35, no. 8, pp. 898–907, Aug. 1990.

[14] W. Rugh and J. S. Shamma, "Research on gain scheduling," *Automatica*, vol. 36, no. 10, pp. 1401–1425, 2000.

[15] H. Köroglu and C. W. Scherer, "LPV control for robust attenuation of non-stationary sinusoidal disturbances with measurable frequencies," *IFAC Proc. Volumes*, vol. 41, no. 2, pp. 4928–4933, 2008.

[16] H. Köroglu and C. W. Scherer, "Scheduled control for robust attenuation of non-stationary sinusoidal disturbances with measurable frequencies," *Automatica*, vol. 47, no. 3, pp. 504–514, Mar. 2011.

[17] C. E. Kinney and R. A. de Callafon, "Scheduling control for periodic disturbance attenuation," in *Proc. Amer. Control Conf.*, 2006, pp. 4788–4793.

[18] C. E. Kinney and R. A. de Callafon, "The internal model principle for periodic disturbances with rapidly time-varying frequencies," *Int. J. Adapt. Control Signal Process.*, vol. 25, no. 11, pp. 1006–1022, Nov. 2011.

[19] H. Du, Z. Lu, X. Shi, and L. Zhang, "LPV technique for the rejection of sinusoidal disturbance with time-varying frequency," *IEE Proc.-Control Theory Appl.*, vol. 150, no. 2, pp. 132–138, Mar. 2003.

[20] K. Zhou, J. C. Doyle, and K. Glover, *Robust and Optimal Control*, vol. 40. Upper Saddle River, NJ, USA: Prentice-Hall, 1996.

[21] M. van de Wal, G. van Baars, F. Sperling, and O. Bosgra, "Ultivariable H_∞/μ feedback control design for high-precision wafer stage motion," *Control Eng. Pract.*, vol. 10, no. 7, pp. 739–755, Jul. 2002.

[22] V. M. Ryaboy, "Practical aspects of design, tuning and application of dynamic vibration absorbers," in *Proc. Meetings Acoust.*, 2016, vol. 26, no. 1, Art. no. 065006.

[23] J. Schoukens, K. Godfrey, and M. Schoukens, "Nonparametric data-driven modeling of linear systems: Estimating the frequency response and impulse response function," *IEEE Control Syst. Mag.*, vol. 38, no. 4, pp. 49–88, Aug. 2018.

[24] L. Ljung and K. Glover, "Frequency domain versus time domain methods in system identification," *Automatica*, vol. 17, no. 1, pp. 71–86, Jan. 1981.

[25] L. Ljung, *System Identification: Theory for the User*, 2nd ed. Upper Saddle River, NJ, USA: Prentice-Hall, 1999.

[26] R. Pintelon and J. Schoukens, *System Identification: A Frequency Domain Approach*, 2nd ed. Hoboken, NJ, USA: Wiley, 2012.

[27] R. A. de Callafon, D. de Roover, and P. M. J. Van den Hof, "Multivariable least squares frequency domain identification using polynomial matrix fraction descriptions," in *Proc. 35th IEEE Conf. Decis. Control*, Mar. 1996, pp. 2030–2035.

[28] T. Oomen and M. Steinbuch, "Identification for robust control of complex systems: Algorithm and motion application," in *Control-Oriented Modelling and Identification: Theory and Applications*. Edison, NJ, USA: IET, 2015.

[29] P. Apkarian, "Nonsmooth μ-synthesis," *Int. J. Robust Nonlinear Control*, vol. 21, no. 13, pp. 1493–1508, Sep. 2011.

[30] P. Apkarian, M. N. Dao, and D. Noll, "Parametric robust structured control design," *IEEE Trans. Autom. Control*, vol. 60, no. 7, pp. 1857–1869, Jul. 2015.

[31] J. S. Shamma, "An overview of LPV systems," in *Control of Linear Parameter Varying Systems with Applications*, J. Mohammadpour and C. W. Scherer, Eds. Boston, MA, USA: Springer, 2012, pp. 3–26, doi: 10.1007/978-1-4614-1833-7_1.

[32] G. F. Franklin, J. D. Powell, and M. L. Workman, *Digital Control of Dynamic Systems*, vol. 3. Reading, MA, USA: Addison-Wesley, 1998.

[33] P. Apkarian, "On the discretization of LMI-synthesized linear parameter-varying controllers," *Automatica*, vol. 33, no. 4, pp. 655–661, Apr. 1997.

[34] R. Toth, M. Lovera, P. S. C. Heuberger, M. Corno, and P. M. J. Van den Hof, "On the discretization of linear fractional representations of LPV systems," *IEEE Trans. Control Syst. Technol.*, vol. 20, no. 6, pp. 1473–1489, Nov. 2012.

[35] S. Skogestad and I. Postlethwaite, *Multivariable Feedback Control: Analysis and Design*. Hoboken, NJ, USA: Wiley, 2005.

[36] E. W. Kamen and B. S. Heck, *Fundamentals of Signals and Systems Using the Web and MATLAB*, 3rd ed. Upper Saddle River, NJ, USA: Prentice-Hall, 2007.